A HIGH-ORDER WEIGHTED RUNGE-KUTTA DISCONTINUOUS GALERKIN METHOD FOR SOLVING 2D ACOUSTIC AND ELASTIC WAVE EQUATIONS IN ISOTROPIC AND ANISOTROPIC MEDIA

XIJUN HE[1,2] and XIAORUI YUE[2]

[1] *Department of Mathematics, School of Mathematics and Statistics, Beijing Technology and Business University (BTBU), Beijing 100048, P.R. China.*
[2] *Department of Mathematics, College of Science, Hainan University, Haikou 570228, P.R. China. yuehd01@sina.com*

(Received November 19, 2018; revised version accepted June 10, 2019)

ABSTRACT

He, X.J. and Yue, X.R., 2019. A high-order weighted Runge-Kutta Discontinuous Galerkin Method for solving 2D acoustic and elastic wave equations in isotropic and anisotropic media. *Journal of Seismic Exploration*, 28: 363-391.

A high-order weighted Runge-Kutta Discontinuous Galerkin Method for solving 2D acoustic and elastic wave equations in isotropic and anisotropic media is proposed in this paper, which is an extension of the existing first-order and second-order methods to higher-order cases. For this method, second-order seismic wave equations are first transformed into a first-order hyperbolic system, then local Lax-Friedrichs (LLF) numerical flux discontinuous Galerkin formulations for spatial discretization are employed, directly leading to a semi discrete ordinary differential equation (ODE) system. For time discretization, an implicit diagonal Runge-Kutta method is introduced. To avoid solving a large-scale system of linear equations, a two-step explicit iterative process is implemented. In addition, a weighting factor is introduced for the iteration to enrich the method. The basis functions we use are $1^{st} \sim 5^{th}$ order polynomials, leading to 2^{nd}- and 6^{th} order of spatial accuracy. Numerical properties of the high-order weighted Runge-Kutta Discontinuous Galerkin Method are investigated in detail, including numerical error, stability criteria and numerical dispersion, which validate the superiority of the high order method. The proposed method is then applied to several 2D wave propagation problems in isotropic and anisotropic media, including acoustic-elastic interface problems. Results illustrate that this method can effectively suppress numerical dispersion and provide accurate information on the wave field on coarse mesh. We also compare the proposed method with the finite difference method to investigate the computational efficiency.

KEY WORDS: seismic wave equation, high-order, Discontinuous Galerkin Method, DGM, weighted, numerical dispersion.

0963-0651/19/$5.00

INTRODUCTION

During the past several decades, the development of computer technology has facilitated huge progress in numerically solving seismic wave equations in complex media. Popular numerical algorithms include finite-difference method (FDM) (Dablain, 1986; Virieux, 1986; Moczo et al., 2000; Yang et al., 2006), finite element method (FEM) (Marfurt, 1984), and spectral element method (SEM) (Komatitsch and Tromp, 1999; Tong et al., 2014), etc. Recently, the Discontinuous Galerkin Method (DGM) has received extensive attention due to its good properties and wide applications. The DGM was first introduced by Reed and Hill (1973) for solving first-order hyperbolic neutron transport equations. Later, the method was extended for solving hyperbolic conservation problems by employing numerical flux formulations and total variation diminishing Runge-Kutta time discretization by Cockburn and Shu (1989, 2001), whose work formulated the Runge-Kutta DGM into a complete mathematical framework. Presently, many kinds of DGMs have been proposed and successfully applied to fluid dynamics (Hesthaven and Warburton, 2007), electromagnetics (Chen and Liu, 2013), and aeroacoustics (Dumbser and Munz, 2005). For more details of these kinds of DGMs, the reader is referred to the unified analysis proposed by Arnold et al. (2002). In computational seismology, DGMs have undergone rapid development (Riviere and Wheeler, 2003; Käser and Dumbser, 2006; Chaljub et al., 2010; Etienne et al., 2010; Minisini et al., 2013; Lambrecht et al., 2017). As a well-known example, Käser and Dumbser (2006) proposed a high order DGM, in which the Riemann flux and a high order derivative time integration method are used. This method retains high order accuracy in space and time, and has been widely used in complicated wave propagation and ground motion (de la Puente et al., 2009; Pelties et al., 2012).

Since DGM can be regarded as a generalization and development of FEM to some degree, many advantageous properties of FEM are inherited. For example, it is easy to deal with domains consisting of complex boundaries for DGM. The stencil of most DGMs is compact, meaning it is associated with only this element and its immediate neighbors without dependence on any other element. Due to a high degree of locality, DGMs can easily process non-conforming meshes and hanging nodes, and can achieve high order accuracy simply by increasing the degrees of basis functions. Moreover, complete localization means that DGMs avoid solving large global mass matrices, making them especially suitable for parallelization.

Most of the developed DGMs are associated to explicit time discretizations, such as Runge-Kutta schemes (Cockburn and Shu, 1989), and the Lax-Wendroff method (Käser and Dumbser, 2006; De Basabe and Sen, 2010). Explicit time-stepping methods are widely used for simple implementation and parallelization. However, there is a strong restriction on

the time step which is known as the Courant-Friedrichs-Lewy (CFL) condition. Implicit solvers, such as diagonally implicit Runge-Kutta (Hairer et al., 2006; Segawa et al., 2011) and Newton iterative methods (Dolejší et al., 2011; Renac et al., 2012), are used in time discretizations because they permit the use of larger time steps. However, the shortcoming for the implicit method is the extremely high computational cost induced by solving large-scale linear algebraic equations. In order to avoid this, some explicit techniques, such as truncated differentiator series method and the predictor-corrector method have been proposed (e.g., Yang et al., 2012; Wang and Zhou, 2014) to turn implicit methods into explicit methods. In this work, implicit diagonal Runge-Kutta formulations for time discretization are introduced, then a two-step explicit iterative process is developed to convert the implicit method to an explicit one.

Follow the work of He et al. (2015), in which the first and second order spatial polynomial interpolations have been considered, here, we consider DGMs with high-order interpolations of 2nd- and 6th order of spatial accuracy and their numerical properties. First, the second-order scalar wave equations are transformed into a first-order hyperbolic system. The numerical approach is then presented in detail, including spatial and time discretizations. Detailed analyses on numerical error, stability condition and numerical dispersion relationship are then discussed. Finally, the high-order weighted Runge-Kutta Discontinuous Galerkin Method is employed to simulate a selection of wave propagation models.

TRANSFORMATION OF THE SEISMIC WAVE EQUATION

In a 2D anisotropic elastic medium, the seismic wave equation can be written as:

$$\rho \frac{\partial^2 U}{\partial t^2} = \left(\frac{\partial}{\partial x}\left(C_1 \frac{\partial}{\partial x} + C_2 \frac{\partial}{\partial z} \right) + \frac{\partial}{\partial z}\left(C_3 \frac{\partial}{\partial x} + C_4 \frac{\partial}{\partial z} \right) \right) \cdot U + f , \tag{1}$$

where $\rho = \rho(x,z)$ is the density, $U = (u_1, u_2)^T$ is the displacement vector, and $f = (f_1, f_2)^T$ is the external force-source vector. Matrices C_1, C_2, C_3, and C_4 are defined as:

$$C_1 = \begin{bmatrix} c_{11} & c_{15} \\ c_{15} & c_{55} \end{bmatrix}, \quad C_2 = \begin{bmatrix} c_{15} & c_{13} \\ c_{55} & c_{35} \end{bmatrix}, \quad C_3 = \begin{bmatrix} c_{15} & c_{55} \\ c_{13} & c_{35} \end{bmatrix}, \quad C_4 = \begin{bmatrix} c_{55} & c_{35} \\ c_{35} & c_{33} \end{bmatrix},$$

where $c_{ij}(x,z)$ are elastic constants. Since this paper is a generalization of the low-order method to the high-order method, most of these notations and variables coincide with He et al. (2014, 2015) in order to facilitate the writing. There are six independent elastic constants $c_{11}, c_{33}, c_{55}, c_{13}, c_{15}, c_{35}$ for the 2D full anisotropic medium. For the isotropic elastic medium, we have two Lamé constants λ and μ, with $c_{33} = c_{11} = \lambda + 2\mu$, $c_{13} = \lambda$, $c_{55} = \mu$ and other elastic constants at zero.

We need some manipulations of eq. (1) to turn it into a 1st-order linear hyperbolic system. Following the transformation in He et al. (2015, 2019), we introduce $P=(p_1,p_2)^T$ and $Q=(q_1,q_2)^T$ satisfied $\frac{\partial P}{\partial t}=\frac{\partial U}{\partial x}$ and $\frac{\partial Q}{\partial t}=\frac{\partial U}{\partial z}$. With the definitions of P and Q, eq. (1) can be rewritten as:

$$\begin{cases} \rho\dfrac{\partial U}{\partial t}=\dfrac{\partial}{\partial x}(C_1P+C_2Q)+\dfrac{\partial}{\partial z}(C_3P+C_4Q)+\tilde{f} \\ \dfrac{\partial P}{\partial t}=\dfrac{\partial U}{\partial x} \\ \dfrac{\partial Q}{\partial t}=\dfrac{\partial U}{\partial z} \end{cases} . \tag{2}$$

Let

$$W=\begin{bmatrix} U \\ P \\ Q \end{bmatrix},\quad F(W)=-\begin{bmatrix} C_1/\rho P+C_2/\rho Q & C_3/\rho P+C_4/\rho Q \\ U & 0 \\ 0 & U \end{bmatrix},\quad \hat{f}=\begin{bmatrix} \tilde{f}/\rho \\ 0 \\ 0 \end{bmatrix},$$

then eq. (2) is simplified to:

$$\frac{\partial W}{\partial t}+\nabla\cdot F(W)=\hat{f} . \tag{3}$$

The unknown vector to be approximated is W, and $F(W)$ is the flux vector. Since the velocity-stress equation is first-order hyperbolic, we say that eq. (3), as well as the algorithm developed below, is also applicable to it.

For the 2D acoustic equation:

$$u_{tt}-c^2(u_{xx}+u_{zz})=f(t) \quad , \tag{4}$$

eq. (3) has a concise form:

$$\begin{bmatrix} u \\ p \\ q \end{bmatrix}_t+\nabla\cdot\begin{bmatrix} -c^2p & -c^2q \\ -u & 0 \\ 0 & -u \end{bmatrix}=\begin{bmatrix} \tilde{f} \\ 0 \\ 0 \end{bmatrix},$$

where c is the acoustic velocity.

NUMERICAL SCHEME

A fully discrete numerical method consists of spatial discretization and time discretization. For the weighted Runge-Kutta Discontinuous Galerkin Method, a detailed description has been described in the literature (He et al., 2015, 2019). Here we present some necessary parts that compose the proposed method.

Spatial discretization

It is assumed that the computational domain $\Omega \in \mathbf{R}^2$ is partitioned into non-overlapping sub-elements $\{\Omega_i\}$. The approximation space for DGM may be discontinuous across element interfaces. In this paper, the scalar test function broken space of the DGM is defined as:

$$V_h = \left\{ v \in L^2(\Omega) : v\big|_{\Omega_i} \in P^{\kappa}(\Omega_i) \right\},$$

where $P^{\kappa}(\Omega_i)$ is a polynomial space of degree at most κ defined on Ω_i. Next we derive the weak form of the solution. Here are some usual practices for DGM. Multiplying eq. (3) by a time-independent scalar test function v and integrating over the sub-element Ω_i gives:

$$\int_{\Omega_i} \left(v \frac{\partial W}{\partial t} + v \nabla \cdot F(W) \right) \mathrm{d}V = \int_{\Omega_i} \hat{f} v \, \mathrm{d}V . \tag{5}$$

Using Green's formula, eq. (5) is recast as:

$$\int_{\Omega_i} \left(v \frac{\partial W}{\partial t} - F(W) \cdot \nabla v \right) \mathrm{d}V + \int_{\partial \Omega_i} v F(W) \cdot n \, \mathrm{d}S = \int_{\Omega_i} \hat{f} v \, \mathrm{d}V , \tag{6}$$

where $\partial\Omega_i$ is the boundary of Ω_i, and n denotes the unit outward normal vector to $\partial\Omega_i$. Eq. (6) is the weak form of eq. (3). The difference between DGM and other numerical methods tells us that W has two possible values: W^{int} and W^{ext}, which are external and internal limits on $\partial\Omega_i$. Then the flux $F(W) \cdot n$ is replaced by the numerical flux $\hat{F}(W^{\text{int}}, W^{\text{ext}}, n)$. The selection of numerical flux is the key to the DG method (LeVeque, 2002). Taking efficiency and robustness into account, the standard LLF numerical flux (Cockburn and Shu, 1989, 2001) is used here, which reads:

$$\hat{F}(W^{\text{int}}, W^{\text{ext}}, n) = \frac{1}{2} \left[F(W^{\text{int}}) + F(W^{\text{ext}}) \right] \cdot n - \frac{C_{\partial\Omega_i}}{2} (W^{\text{ext}} - W^{\text{int}}), \tag{7}$$

where the numerical viscosity constant $C_{\partial\Omega_i}$ can be taken as be the largest eigenvalue between $\left| \frac{\partial}{\partial W} F(W^{\text{int}}) \cdot n \right|$ and $\left| \frac{\partial}{\partial W} F(W^{\text{ext}}) \cdot n \right|$.

Let's consider the basis function expansions of W. Suppose $\left\{w_l^i\right\}_{l=1}^{l=d_{loc}}$ is a set of basis functions for DGM, where d_{loc} is the number of local degree of freedom (DOF) per element. There are two kinds of basis functions, order-complete basis and tensor-product basis (Hu et al., 1999), the number of DOF for which is $d_{loc}=\frac{(\kappa+1)(\kappa+2)}{2}$ for the order-complete basis and $d_{loc}=(\kappa+1)^2$ for the tensor-product basis. In this study, we use order-complete basis, so $d_{loc}=\frac{(\kappa+1)(\kappa+2)}{2}$. Here, the Legendre basis polynomials are employed for the numerical analysis and the simulations on regular quadrilateral mesh. For triangular elements, there are also orthogonal basis functions, but the expressions are more complicated. In this study, we choose $\left\{x^\alpha z^\beta \,|\, 0\le\alpha+\beta\le\kappa\right\}$ as the basis functions, which are easy to calculate for high orders, and the related condition number of the mass matrix is within the acceptable range. The numerical solution of eq. (6) could be approximated as:

$$W\big|_{\partial\Omega_i}=\sum_{l=1}^{d_{loc}}c_l^i(t)w_l^i\,, \tag{8}$$

in which $\left\{c_l^i(t)\right\}_{l=1}^{d_{loc}}$ are time dependent coefficients. With eq. (8), we replace v with $w_{l'}^i$ in eq. (6), so that eq. (6) reads as

$$\begin{aligned}\sum_{l=1}^{d_{loc}}\frac{\partial c_l^i(t)}{\partial t}\int_{\Omega_i}w_l^iw_{l'}^i\,\mathrm{d}V-\int_{\Omega_i}F\left(\sum_{l=1}^{d_{loc}}c_l^i(t)w_l^i\right)\cdot\left(\frac{\partial w_{l'}^i}{\partial x},\frac{\partial w_{l'}^i}{\partial z}\right)\mathrm{d}V\\ +\sum_j\int_{\Omega_i\cap\Omega_j}w_{l'}^i\hat{F}\left(\left(\sum_{l=1}^{d_{loc}}c_l^i(t)w_l^i\right),\left(\sum_{l=1}^{d_{loc}}c_l^j(t)w_l^j\right),n\right)\mathrm{d}S=\int_{\Omega_i}\hat{f}w_{l'}^i\,\mathrm{d}V\end{aligned}\,. \tag{9}$$

In eq. (9) the superscript j denotes the values taken from the adjacent element. Note that all integrals appearing in eq. (9) are calculated by means of numerical integration. It is suggested that the quadrature rule for the edge

integrals should be exact for polynomials of degree at least $2\kappa+1$, and for the element integrals it should be exact for polynomials of degree at least 2κ (Cockburn and Shu, 1998, 2001).

Time discretization

After spatial discretization, a semi discrete ODE system remains to solve. To simplify the expression, a coefficient vector $C^i(t)$ is introduced to represent the coefficients $\left\{c_l^i(t)\right\}_{l=1}^{d_{loc}}$. The element superscript i and the time term t are both omitted. Then, the semi discrete eq. (9) has a compact notation, which reads

$$\frac{\partial C}{\partial t} = L(C) + \bar{F}, \tag{10}$$

where L is the linear operator with respect to DG spatial discretization and $\bar{F}$ denotes the source excitation item.

To relax the CFL stability conditions, the following implicit diagonal Runge-Kutta method is used to solve system (10):

$$C^{(n+1)} = C^{(n)} + \frac{\Delta t}{2}(K^{(n)} + \bar{K}^{(n)}), \tag{11}$$

$$K^{(n)} = L(C^{(n)} + r\Delta t K^{(n)}) + \bar{F}(t^n + r\Delta t), \tag{11a}$$

$$\bar{K}^{(n)} = L(C^{(n)} + (1-2r)\Delta t K^{(n)} + r\Delta t \bar{K}^{(n)}) + \bar{F}(t^n + (1-r)\Delta t). \tag{11b}$$

where $r = \left(3-\sqrt{3}\right)/6$.

Obviously, scheme (11) is an implicit scheme. In the Introduction section, we have discussed the shortcomings of implicit method, therefore, we decide to convert this implicit method into an explicit one. Following the techniques proposed by He et al. (2014, 2015, 2019), we use an iteration procedure. If the source item is ignored, eq. (11a) implies the following iteration process when $\left\|r\Delta t L\right\| < 1$:

$$K_{k+1}^{(n)} = r\Delta t L(K_k^{(n)}) + L(C^{(n)}),\ k = 0,1,2,\mathrm{K}\quad, \tag{12}$$

where the subscript k denotes the iteration number. Now we will discuss the selection of the initial value for $K^{(n)}$ in eq. (12). From eq. (11) we know that both $K^{(n)}$ and $\bar{K}^{(n)}$ are reasonable approximations of $L(C^{(n)})$, so we

can choose $L(C^{(n)})$ as the iterative initial value for $K^{(n)}$ and $\bar{K}^{(n)}$.We implement a two-step iterations for eq. (12) are implemented in the form:

$$\begin{cases} K_0^{(n)} = L(C^{(n)}) \\ K_1^{(n)} = r\Delta t L(K_0^{(n)}) + L(C^{(n)}) \\ K_2^{(n)} = r\Delta t L(K_1^{(n)}) + L(C^{(n)}) \end{cases} . \tag{13}$$

To enrich the numerical method, we take a weighted combination of $K_2^{(n)}$ and $K_1^{(n)}$ for the approximation of $K^{(n)}$, being:

$$K^{(n)} = \eta K_2^{(n)} + (1-\eta)K_1^{(n)} = L(C^{(n)}) + r\Delta t L^2(C^{(n)}) + \eta(r\Delta t)^2 L^3(C^{(n)}) . \tag{14}$$

Here the weighting factor is $\eta \in [0,1]$. The same process as in eq. (14) is then implemented to calculate $\bar{K}^{(n)}$. It is worth mentioning that both $L(T^{(n)})$ and $L(C^{(n)})$ can be used as the initial value of $\bar{K}^{(n)}$.

ERROR ANALYSIS, STABILITY CRITERIA AND NUMERICAL DISPERSION

In this section, the numerical errors of the proposed method are initially investigated, then Von Neumann analysis is applied to discuss its stability and numerical dispersion.

Error analysis

To further illustrate the numerical spatial accuracy of the high-order weighted Runge-Kutta Discontinuous Galerkin Method, the 2D homogeneous acoustic wave equation in eq. (4) is considered, with the exact solution:

$$\begin{cases} u(t,x,z) = \cos\left(2\pi f_0 t - \dfrac{2\pi f_0}{c}\cos\theta_0 x - \dfrac{2\pi f_0}{c}\sin\theta_0 z\right) \\ p(t,x,z) = -\dfrac{\cos\theta_0}{c}\cos\left(2\pi f_0 t - \dfrac{2\pi f_0}{c}\cos\theta_0 x - \dfrac{2\pi f_0}{c}\sin\theta_0 z\right), \\ q(t,x,z) = -\dfrac{\sin\theta_0}{c}\cos\left(2\pi f_0 t - \dfrac{2\pi f_0}{c}\cos\theta_0 x - \dfrac{2\pi f_0}{c}\sin\theta_0 z\right) \end{cases} \tag{15}$$

where c is the acoustic velocity, θ_0 denotes the incident direction at time t = 0, and f_0 is the peak frequency. We quote this example from He et al. (2015).

The parameter settings for this example are similar to that in He et al. (2015), but here we will consider the high-order cases. We set $0 \le x, z \le 1.414$ km, $c = 4$ km/s, $f_0 = 20$ Hz, and $\theta_0 = \pi/4$. The time step is set to be $\Delta t = 0.1$ ms such that the numerical errors caused by the time discretization can be ignored, hence the errors are dominated by the spatial discretization errors. We run 1000 time iterations for all the simulations. In this numerical test, the value of the weight η is found to have little effect on the numerical errors, therefore a simplified $\eta = 1.0$ is used in the numerical modeling.

The continuous L^1 and L^2 norm errors between the numerical solution u_h and the exact solution u are defined as:

$$E_{L^k} = \left\| u_h - u \right\|_{L^k} = \left(\int_\Omega \left| u_h - u \right|^k d\Omega \right)^{\frac{1}{k}}, k = 1, 2\text{K} .$$

Table 1. Convergence rates of u in spatial discretization for $P^1 \sim P^5$ basis functions.

	h	L^2 error	order	L^1 error	order	DOF	CPU(s)
P^5	3.928E-02	9.150E-06	-	9.386 E-06	-	8.165E+04	9.680E+02
	4.714E-02	2.605E-05	5.738	2.709E-05	5.814	5.670E+04	6.794E+02
	5.238E-02	4.858E-05	5.803	4.995E-05	5.807	4.593E+04	5.456E+02
	7.857E-02	5.362E-04	5.922	5.672E-04	5.992	2.041E+04	2.421E+02
P^4	2.828E-02	2.636E-05	-	2.837E-05	-	1.125E+05	9.870E+02
	3.143E-02	4.427E-05	4.922	4.829E-05	5.050	9.113E+04	8.033E+02
	3.928E-02	1.327E-04	4.920	1.453E-04	4.936	5.832E+04	5.116E+02
	7.857E-02	3.803E-03	4.840	4.217E-03	4.859	1.458E+04	1.290E+02
P^3	1.964E-02	9.676E-05	-	1.066E-04	-	1.555E+05	9.632E+02
	2.357E-02	1.976E-04	3.915	2.169E-04	3.897	1.080E+05	6.682E+02
	3.143E-02	6.040E-04	3.885	6.660E-04	3.899	6.075E+04	3.759E+02
	3.928E-02	1.430E-03	3.861	1.572E-03	3.850	3.888E+04	2.428E+02
P^2	1.179E-02	3.349E-04	-	3.524E-04	-	2.592E+05	1.062E+03
	1.571E-02	8.035E-04	3.042	8.627E-04	3.112	1.458E+05	5.915E+02
	1.964E-02	1.602E-03	3.093	1.765E-03	3.209	9.331E+04	3.798E+02
	3.928E-02	1.676E-02	3.387	2.087E-02	3.564	2.333E+04	9.647E+01
P^1	7.857E-03	5.671E-03	-	6.347E-03	-	2.916E+05	7.323E+02
	1.571E-02	3.893E-02	2.779	4.796E-02	2.918	7.290E+04	1.802E+02
	3.143E-02	3.407E-01	3.129	4.331E-01	3.175	1.823E+04	6.789E+01
	3.928E-02	5.344E-01	2.018	6.788E-01	2.014	1.166E+04	4.365E+01

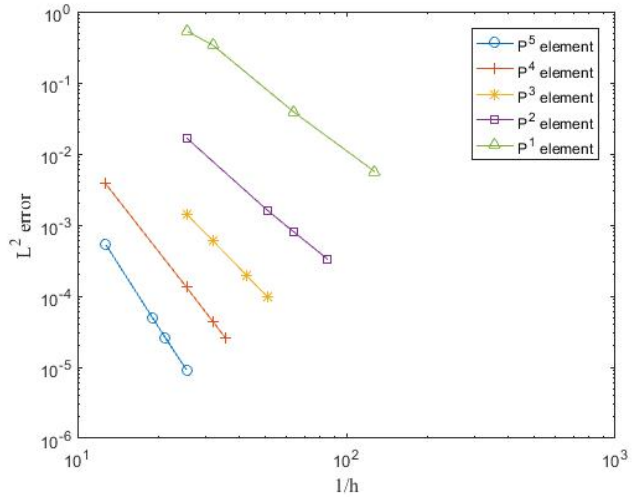

(a)

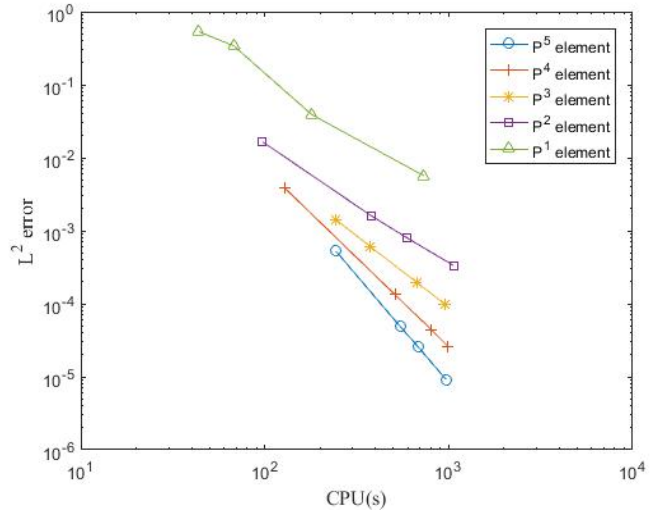

(b)

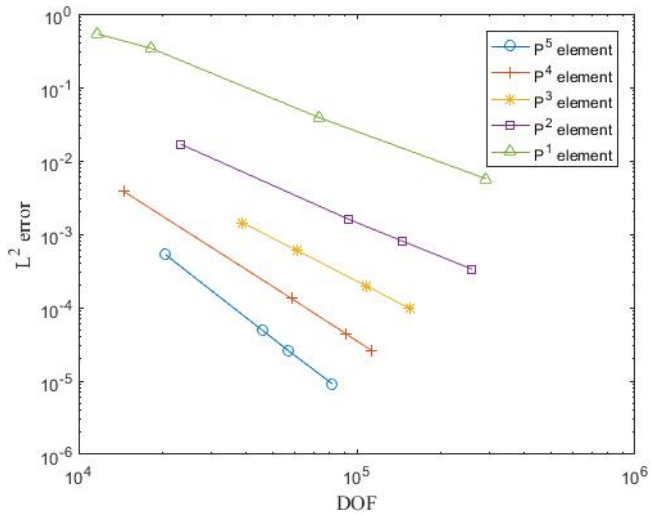

(c)

Fig. 1. (a) Numerical errors versus mesh size 1/ h; (b) Numerical errors versus size of DOFs; (c) Numerical errors versus CPU times. We consider $P^1 \sim P^5$ basis functions for spatial discretization.

Table 1 shows the L^1 and L^2 numerical errors and convergence orders in relation to mesh size h. The basis functions $P^1 \sim P^5$ are considered for spatial discretization. Furthermore, the size of DOFs and CPU times are listed for simulating these cases, which are measurements of the required storage and calculation speed, respectively. From Table 1 it can be observed that the proposed method with P^κ elements is convergent and achieves the expected (κ+1)-th order of accuracy for $\kappa = 1, 2, 3, 4, 5$.

In this study we focus on the high-order cases. It can be seen from Table 1 that the numerical error of the higher order method is much smaller than that of the lower order method. To compare the computational efficiency for all the cases, we plot the L^2 errors varying with grid step size, storage and CPU times for different orders in Fig. 1. As can be seen, when the same mesh size is used, or given the same amount of storage and CPU times, the numerical errors produced by the higher-order method are significantly reduced, which fully demonstrates the advantages of the higher order method. Therefore, for large-scale modelling, the high-order method can use coarse grids, which greatly reduces the amount of storage and calculations, hence improves the computational efficiency.

Stability conditions

Stability conditions for the high order weighted Runge-Kutta Discontinuous Galerkin Method are considered here. This analysis is based on the Von Neumann analysis, which has been presented in detail in He et al. (2015, 2019). Here we just present it in the Appendix A, where the eigenvalue Λ of the growth matrix for the algorithm in eq. (A-6) has been deduced. From the definition of Λ, we know that to keep the scheme stable, Λ must satisfy $|\Lambda| \le 1$ for all eigenvalues, all wave numbers $kh \in [0, \pi]$ and for all propagation directions $\theta \in [0, 2\pi]$. Table 2 shows the different maximum Courant numbers for P^κ (κ = 1, 2, 3, 4, 5) elements for different weights η from 0 to 1. It is observed that the maximum Courant numbers are obtained when η is taken to be some intermediate value between 0 and 1.

Table 2. Approximate maximum Courant numbers for different weights.

η	0.0	0.1	0.2	0.3	0.4	0.5	0.6	0.7	0.8	0.9	1.0
P^1	0.592	0.668	0.818	1.040	0.982	0.784	0.676	0.610	0.562	0.528	0.5
P^2	0.224	0.232	0.242	0.254	0.270	0.292	0.324	0.32	0.294	0.276	0.262
P^3	0.184	0.191	0.200	0.210	0.223	0.240	0.238	0.214	0.198	0.186	0.176
P^4	0.121	0.126	0.131	0.138	0.146	0.157	0.162	0.146	0.135	0.126	0.120
P^5	0.089	0.092	0.096	0.101	0.106	0.114	0.121	0.109	0.100	0.094	0.089

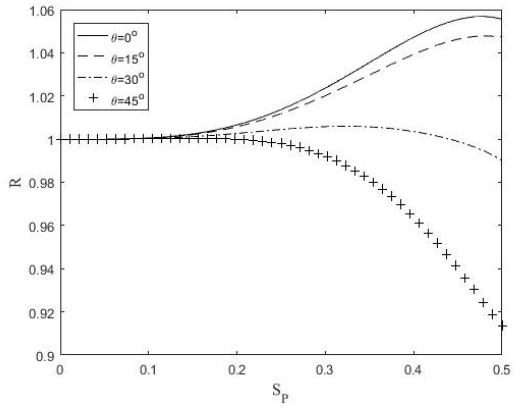

(a)

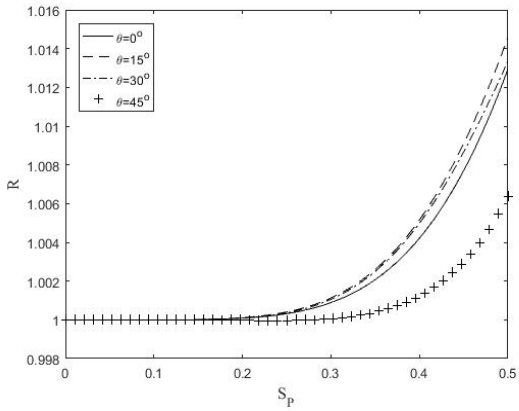

(b)

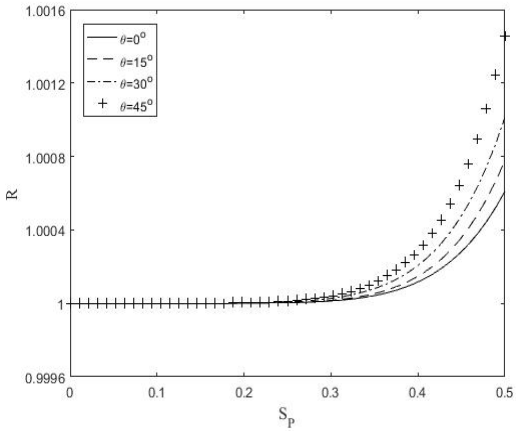

(c)

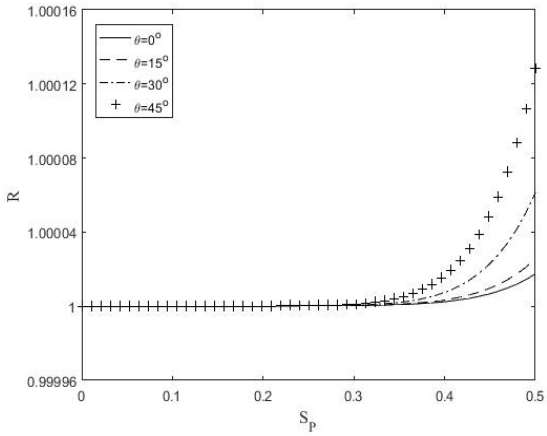

(d)

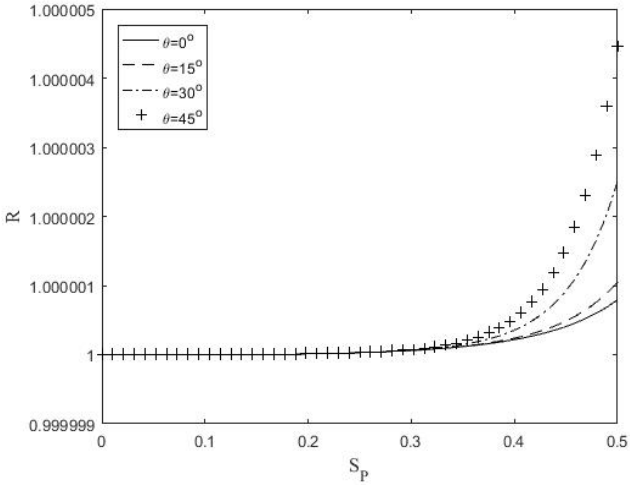

(e)

Fig. 2. Numerical dispersion R as a function of the spatial sampling ratio S_p when $\theta = 0^\circ, 15^\circ, 30^\circ, 45^\circ$. (a) ~ (e) $P^1 \sim P^5$ basis functions for spatial discretization.

Note that the stability conditions for the heterogeneous media cannot be directly determined but could be approximated by using the maximum wave velocity c in the homogeneous case. In addition, the basis function used here is order-complete basis, not tensor-product basis. If tensor product basis was to be used, the size of DOFs for each element would increase, and the stability condition would be more rigorous.

Dispersion analysis

Numerical dispersion occurs when the numerical method is used to discretize the wave equation. In this subsection, the numerical dispersion including the effects of space and time discretizations are investigated. The analysis is based on the Von Neumann analysis in Appendix A.

Fig. 2 shows how numerical dispersion R varies with the sampling ratio $S_p \in [0, 0.5]$ for $P^1 \sim P^5$ elements. The results for four propagation directions $\theta = 0^\circ, 15^\circ, 30^\circ, 45^\circ$ are presented here. These results are computed with $\eta = 1.0$ and $\alpha = 0.1$, except for P^5 elements where $\alpha = 0.08$ is used to satisfy its stability condition. Figs. 2(a)-(e) show that numerical dispersion is significantly decreased as the order of spatial discretization increases, especially for $\kappa > 2$; in particular, we see that when $\kappa = 5$ and $S_p = 0.5$, the dispersion error is less than 5×10^{-6}. Meanwhile, it can be observed that for P^1 element, the numerical dispersion oscillates around 1 for different θ, which implies that the waves are delayed or advanced according to different propagation directions. However, for $P^2 \sim P^5$ elements, the numerical dispersion R is slightly greater than 1 for all propagation directions, meaning that the waves are slightly advanced.

The anisotropy of the numerical dispersion is displayed in Fig. 3, where results for sampling ratios $S_p = 0.4, 0.45, 0.5$ are provided. The parameters for the weighting factor and Courant number are the same as in Fig. 2. It can be seen from Fig. 3 that numerical dispersion is strongly related to the propagation angle θ. However, since the numerical dispersion for high-order schemes (especially for $\kappa > 2$) is very small, the whole anisotropy is also very small.

NUMERICAL SIMULATIONS

In this section, we present some numerical examples to further illustrate the correctness and capability of the high-order weighted Runge-Kutta Discontinuous Galerkin Method.

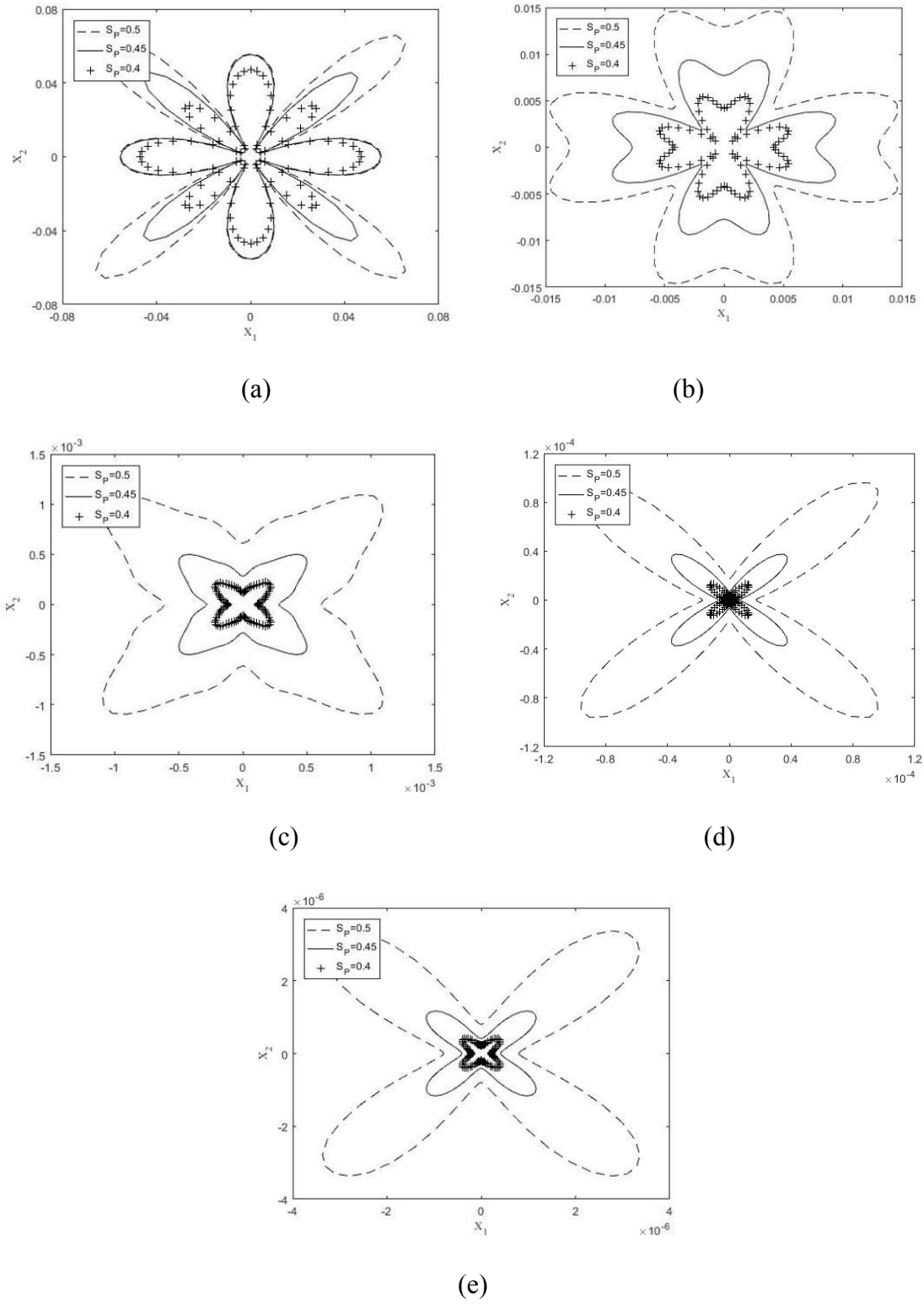

Fig. 3. Anisotropy curves of numerical dispersion R with the spatial sampling ratio $S_p = 0.5,\ 0.45,\ 0.4$. (a) ~ (e) $P^1 \sim P^5$ basis functions for spatial discretization.

Homogeneous acoustic model

To investigate the validity of the proposed method in suppressing numerical dispersion on a coarse mesh, a 2D homogeneous acoustic model with the velocity of c = 3.0 km/s is used. The computational region is $0 \le x, z \le 10$ km. The explosive source frequency in eq. (4) is a Ricker wavelet:

$$f(t) = -5.76 f_0^2 [1 - 16(0.6 f_0 t - 1)^2] \exp[-8(0.6 f_0 t - 1)^2], \tag{16}$$

with peak frequency f_0 = 24 Hz. The source is located at the center of the domain with a receiver at (6 km, 6 km) to observe the waveforms. For this example, a 4th-order weighted Runge-Kutta discontinuous Galerkin scheme with $\eta = 0.5$ is used. A uniform grid spacing of the size 50 m × 50 m with $\Delta t = 3.8$ ms is selected for computation, resulting in about 2.5 elements per minimum wavelength.

In Fig. 4, the snapshot of the displacement at T = 1.2 s is presented, wherein no visible numerical dispersion can be observed. To illustrate the precise match between the numerical solution and the analytical solution, we present the normalized waveforms at the receiver in Fig. 5. The solid line denotes the analytical solution computed by the Cagniard-de Hoop method (Aki and Richards, 2002), and the dashed line represents the numerical solution computed by the proposed method. Fig. 5 indicates that the numerical solution corresponds well with the analytic solution, illustrating that the proposed method can provide almost the same result as the analytical solution. Additionally, no visible numerical dispersion from the waveforms is observed in Fig. 5. The test shows that the proposed method can effectively suppress the numerical dispersion on the coarse grid.

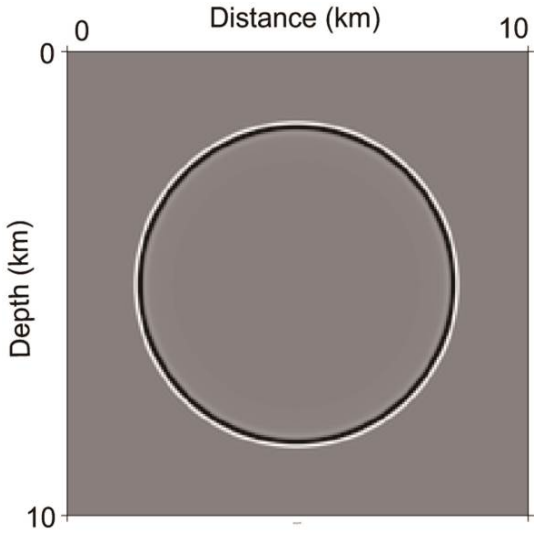

Fig. 4. Snapshot of the seismic wave fields at time $T = 1.2$ s for the homogeneous acoustic medium with a uniform grid spacing of 50 m.

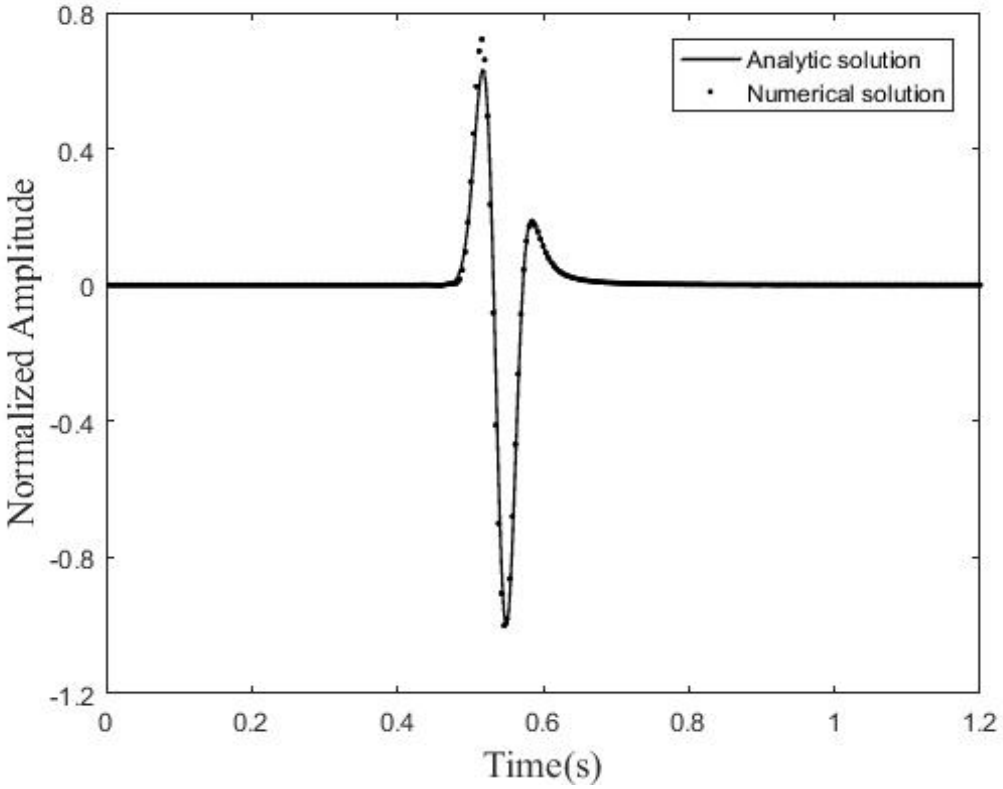

Fig. 5. Waveforms of the seismic wave fields at time $T = 1.2$ s generated by the 4th-order weighted Runge-Kutta Discontinuous Galerkin Method (dotted line), and the reference solution (solid line) for the homogeneous medium.

Three-layer model

In this example, a three-layer model with a computational domain of $0 \le x, z \le 6$ km is selected. The velocity is 3.0 km/s in the top layer where $0 \le z \le 1.5$ km, 2.0 km/s in the middle layer where $1.5 \le z \le 3.3$ km, and 4.0 km/s in the bottom layer. The source, located at (3 km, 2.655 km), is a Ricker wavelet with source function as in eq. (16). The peak frequency is 32 Hz. Two receivers are also set, located at R1 (3 km, 1.815 km) and R2 (4.2 km, 4.215 km) to observe the waveforms. The spatial and temporal increments selected are 30 m and $\Delta t = 1.8$ ms, respectively. For the purpose of comparison, this model is also simulated by the commonly used FDM-Lax-Wendroff correction (LWC) method (Dablain, 1986). Fig. 6 shows the snapshots at $T = 1.0$ s generated by the 4th-order weighted Runge-Kutta discontinuous Galerkin scheme with a weighting factor of $\eta = 0.5$ and the 4th-order LWC method for the same computational parameters. The wave propagation phenomena including reflection and transmission can be clearly observed in Fig. 6(a) without visible numerical dispersion, whereas the LWC method [Fig. 6(b)] suffers from serious numerical dispersion.

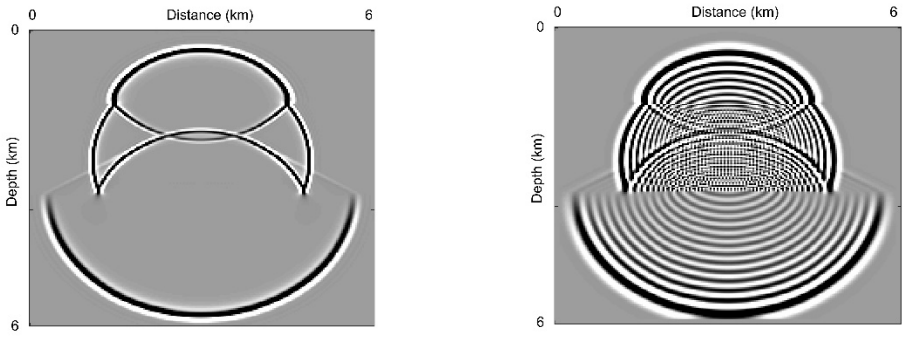

(a) (b)

Fig. 6. Snapshots of the seismic wave fields at time $T = 1.0$ s for the three-layer model with a uniform grid spacing of 30 m. (a) 4th-order weighted Runge-Kutta Discontinuous Galerkin Method; (b) 4th-order LWC method.

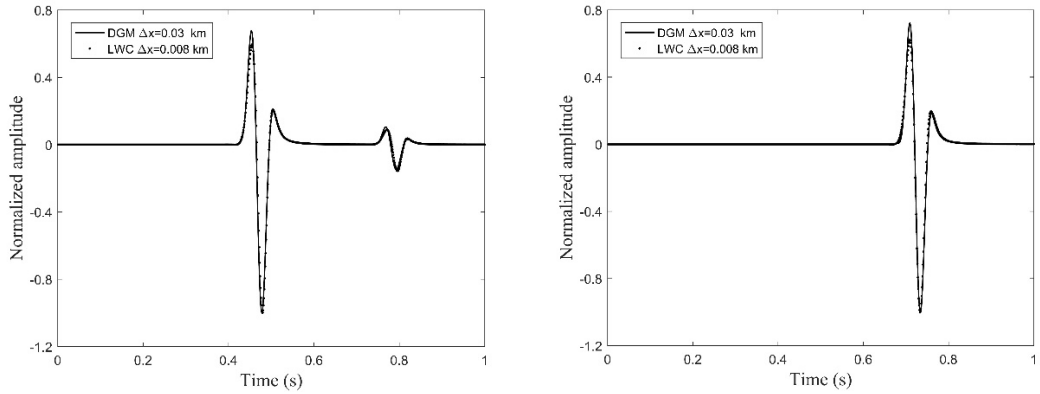

(a) (b)

Fig. 7. Comparisons of the waveforms for u at two receivers in the three-layer model at time $T = 1.0$ s, generated by the 4th-order weighted Runge-Kutta Discontinuous Galerkin Method (30 m × 30 m) and the 4th-order LWC method (8 m × 8 m). (a) R1; (b) R2.

In order to eliminate the numerical dispersion and offer an accurate view of the wave field, the LWC method is implemented using a finer grid ($\Delta x = \Delta z = 8$ m). With the finer grid the LWC method produces almost no numerical dispersion. The waveforms are shown at the two receivers. From Fig. 7 it can be seen that the proposed method can provide almost the same solution on a much coarser grid as that of the LWC method on a finer grid. It must be noted that although the proposed method produces smaller numerical dispersion on the coarse grid, its computation time is much greater than the LWC method. For this model, it takes about 3995 seconds for the weighted Runge-Kutta Discontinuous Galerkin Method to generate the results in Fig. 7 on a coarse grid, whereas it takes only 95 seconds for the LWC method to generate the same results on a fine grid. This is a computing time gap of approximately 42 times between the two methods. Therefore, how to improve the calculation speed of the proposed method is a challenge

for future development, and the main issue to be considered by the authors in the future.

Cave model

In this example, acoustic wave propagation in a cave is simulated, and the cave model is presented in Fig. 8. The computational region is $0 \le x, z \le$ 5.6 km. There is a circular cave with the radius 0.5 km in the background medium with the center located at (2.8 km, 4.2 km). The source, located at the center of the domain, is a Ricker wavelet with source function as in eq. (16). The peak frequency is 30 Hz. The velocity in the homogeneous background medium is 4.0 km/s, whereas the velocity in the cave is 1.5 km/s. The global grid size is about 40 m, and in the cave the average edge length of the triangular mesh is about 15 m. Part of the irregular triangular mesh is shown in Fig. 9. For the result shown in this example, a 4th-order scheme with $\eta = 0.5$ and $\Delta t = 0.38$ ms is used. Snapshots at T = 0.3, 0.4, 0.6 and 0.7 s for the cave model are illustrated in Fig. 10, where the wave's arrival, reflection and transmission caused by the existence of the cave is clearly visible. The snapshots are very clear and have no visible numerical dispersion. This model demonstrates that the suggested method can simulate wave propagation in complex structures with large velocity contrast.

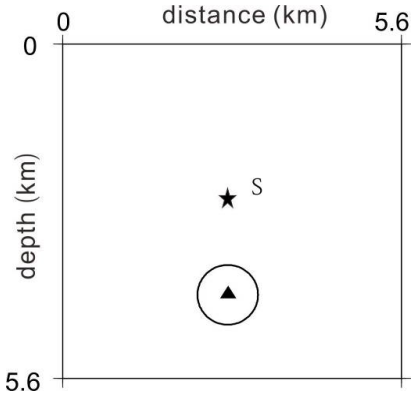

Fig. 8. Illustration of the cave model. There is a circular cave of radius 0.5 km in the background medium with the center located at (2.8 km, 4.2 km). The source, denoted by *S*, is located at the center of the domain.

Isotropic and anisotropic elastic media

In this example, elastic wave propagation in 2D isotropic and anisotropic media is investigated through the consideration of three separate cases. The elastic parameters for Cases 1 and 2 are presented in Table 3. For Case 3, there is a horizontal interface at the center of the *z*-direction in the medium, with the parameters of the lower and upper layers similar to those of Case 1

and Case 2, respectively. The computational region is $0 \le x, z \le 7.5$km. The source is located at the center of the domain for Case 1 and Case 2, while for Case 3 the source coordinate is (3.75 km, 4.125 km). The source function is the same as in eq. (16), with a peak frequency of 15 Hz. The computational domain is discretized by 22887 triangles with an average edge length of 0.07 km. The time step is $\Delta t = 0.43$ ms and a 4th-order weighted Runge-Kutta Discontinuous Galerkin Method scheme with $\eta = 0.5$ is implemented.

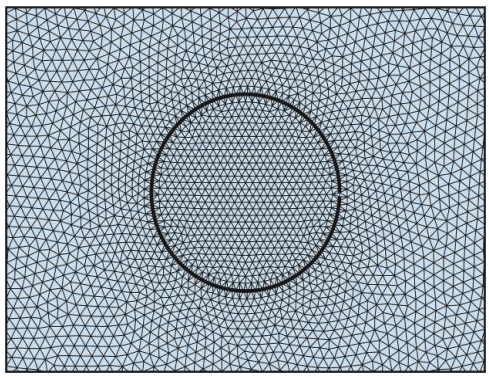

Fig. 9. Irregular mesh for the cave and its surroundings.

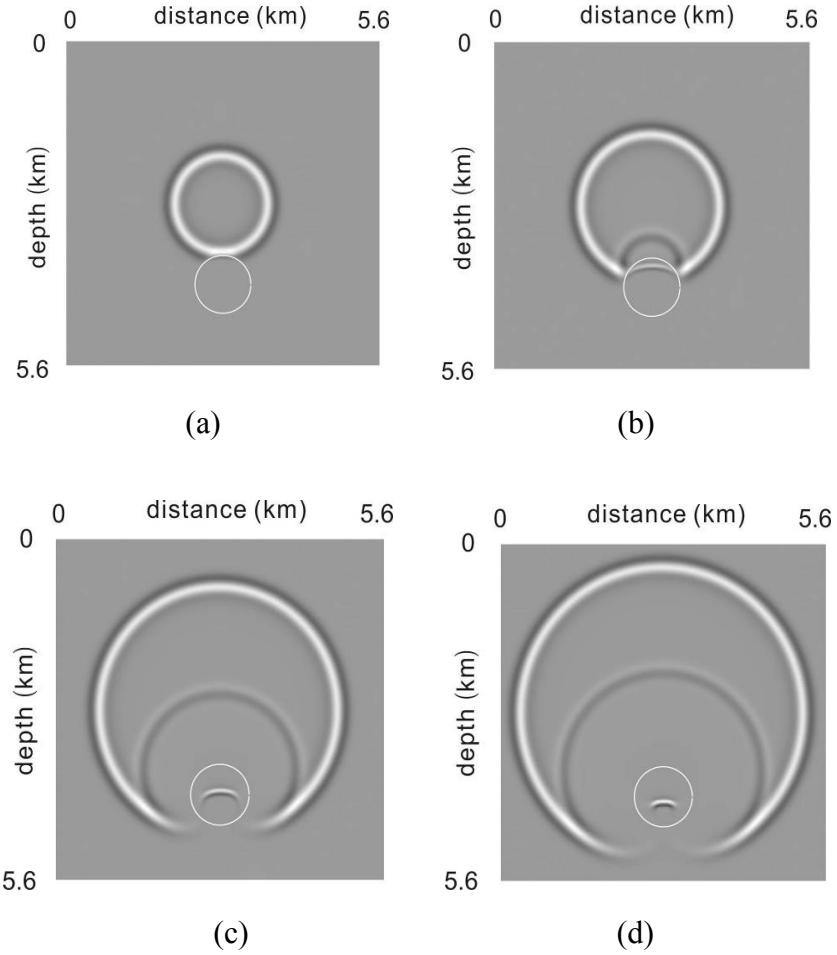

Fig. 10. Snapshots for the cave model at time (a) $T = 0.3$ s, (b) $T = 0.4$ s, (c) $T = 0.6$ s, and (d) $T = 0.7$ s.

Table 3. Parameters for the isotropic and anisotropic elastic media.

	C_{11} (GPa)	C_{13} (GPa)	C_{33} (GPa)	C_{44}(GPa)	ρ (g/cm^3)
Case 1	13.14	4.38	13.14	4.38	2.1
Case 2	25.2	6.11	15.0	4.38	2.1

Fig. 11 presents the wavefield snapshots of the displacement vector (u_1,u_2) at $T = 1.0$ s for the three cases. The propagation for the *P*-wave and *S*-wave are clearly observed in Figs. 11(a) and 11(d). Additionally, the cusps and the anisotropy of the wave propagation are visible in Figs. 11(b) and 11(e). In Figs. 11(c) and 11(f), the propagation of the direct *P*-wave and direct *S*-wave are evident. Similarly, the reflected, transmitted, and converted waves caused by the interface can be also clearly identified from the snapshots. The snapshots are clear with no visible numerical dispersion. The results show that the proposed method performs well for complicated wave propagation phenomena in isotropic and anisotropic media.

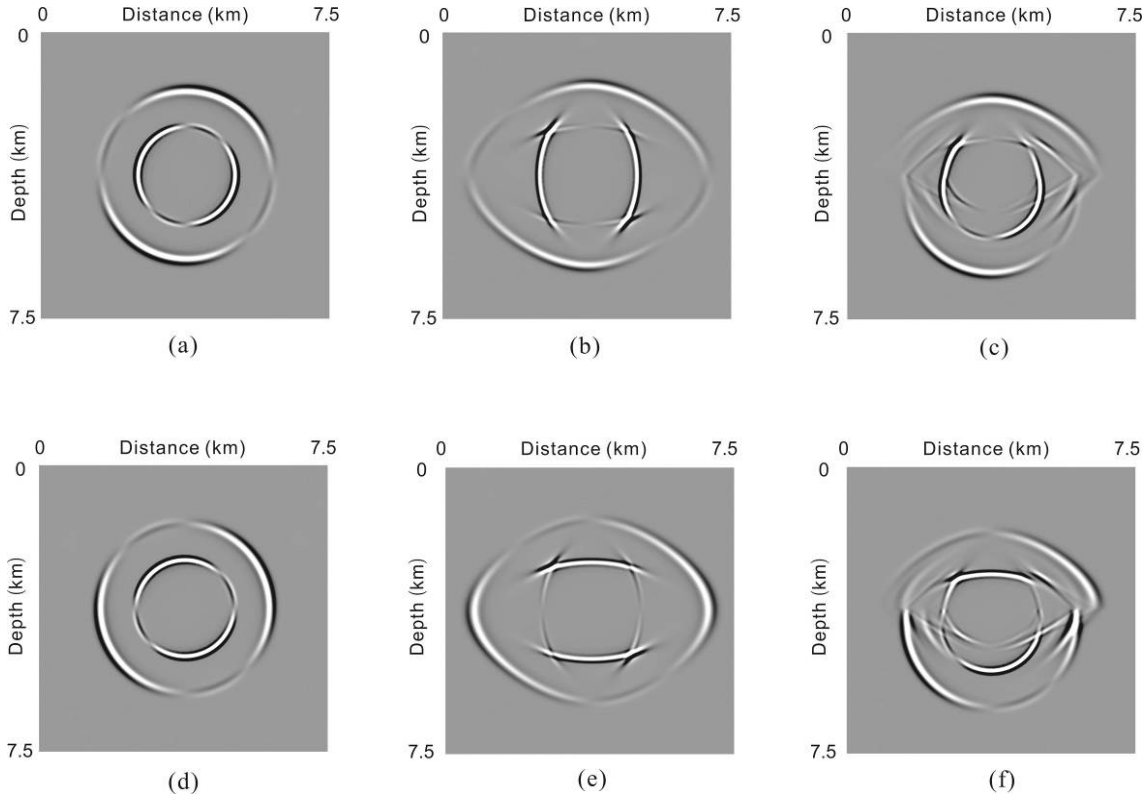

Fig. 11. Snapshots for the displacements (u_1,u_2) in the isotropic and anisotropic elastic media at time $T = 1.0$ s. (a) and (d) are the snapshots for Case 1 (the isotropic elastic model); (b) and (e) are the snapshots for Case 2 (the anisotropic elastic model); (c) and (f) are the snapshots for Case 3 (the two-layer model).

Acoustic-elastic interface

In this example, acoustic-elastic interface problems are examined. In the real world, the fluid-solid interface could represent the water layer on a rock layer, and is of major importance in marine exploration seismology (Zhang, 1997; Käser and Dumbser, 2008). Two models are considered here. The first model has a plat interface, while the second has a sinusoidal interface. The two models and some parameters are illustrated in Fig. 12 (Zhang, 1997). The wavelength of the sinusoidal interface is 200 m with an amplitude of 30m. The source is located at (2 km, 2.3 km) with the same function as in eq. (16), and f_0 = 20 Hz. The interface is located at z = 2 km. For the first model, the computational domain is discretized by 29742 triangles with an average edge length of 0.03 km; for the second model, there are 25672 triangles, and the length of the grid near the interface is about 0.02 km. The 4th-order scheme with $\eta = 0.5$ is used with a time step of 0.4 ms.

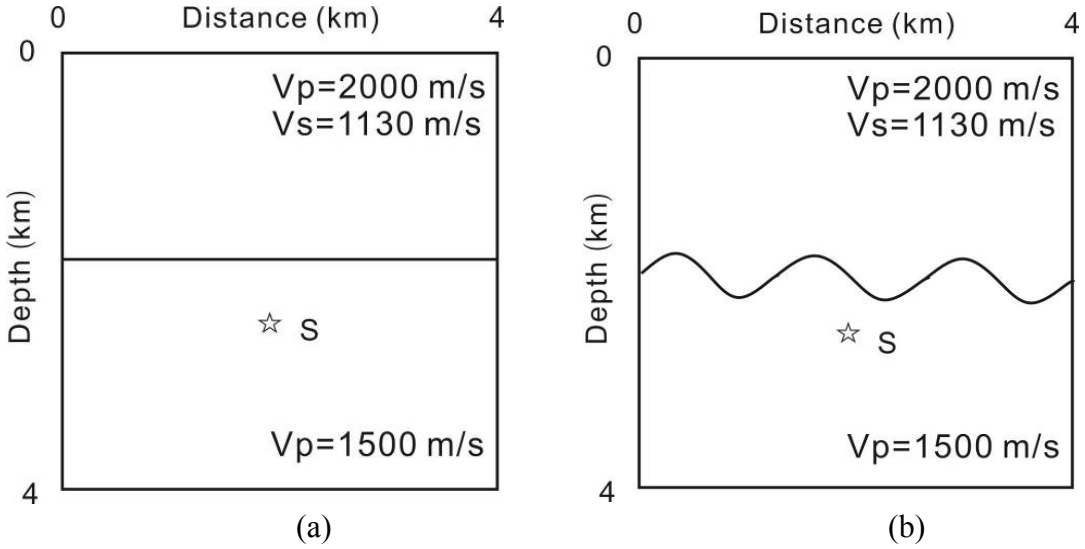

Fig. 12. Illustrations of the acoustic-elastic interface model. (a): horizontal interface; (b): sinusoidal interface.

Fig. 13 shows the wave-field snapshots of the displacement vector (u_1,u_2)at $T = 0.5$ s, 0.8 s and 1.1 s for Model 1. The direct and reflected acoustic waves are clearly visible in the fluid domain. In the solid domain, the transmitted *P*-wave with the converted *S*-wave can be clearly observed. In contrast, Fig. 14 shows the wave-field snapshots for the sinusoidal acoustic-elastic interface. In addition to the visible wave phenomena in Fig.13, a series of scattering waves are visible in Fig. 14 due to the sinusoidal tomography. The snapshots are clear without visible numerical dispersion. The results show that the weighted Runge-Kutta Discontinuous Galerkin Method performs well for complicated wave propagation phenomena in acoustic-elastic interface problems.

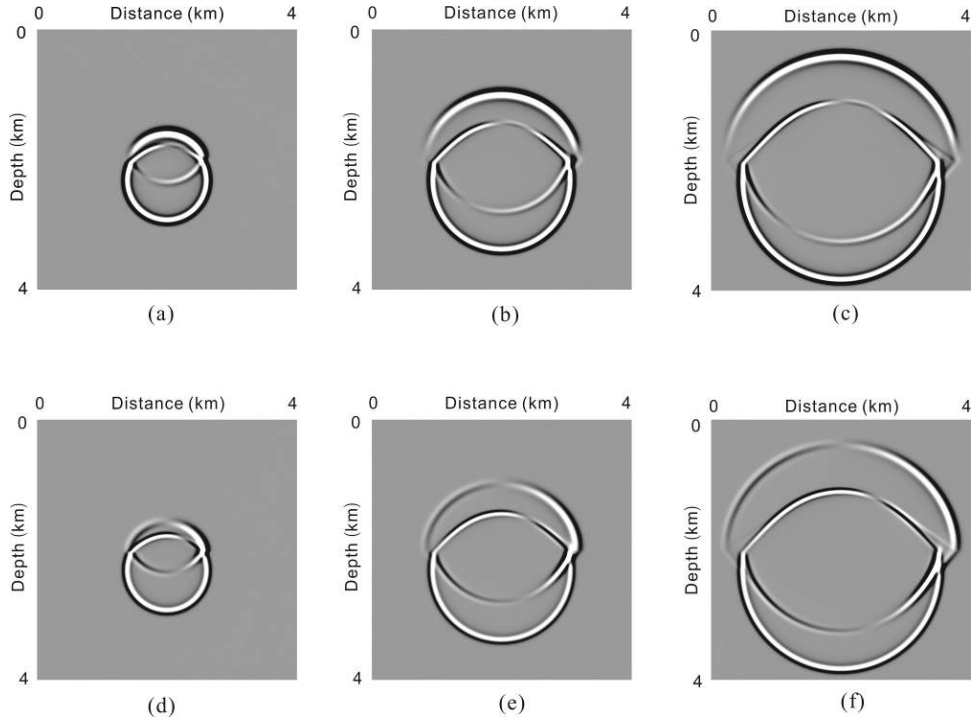

Fig. 13. Snapshots for the displacements (u_1, u_2) in the horizontal acoustic-elastic interface model at time $T = 0.5$ s, $T = 0.8$ s and $T = 1.1$ s. (a) and (d) are the snapshots for $T = 0.5$ s; (b) and (e) are the snapshots for $T = 0.8$ s: (c) and (f) are the snapshots for $T = 1.1$ s.

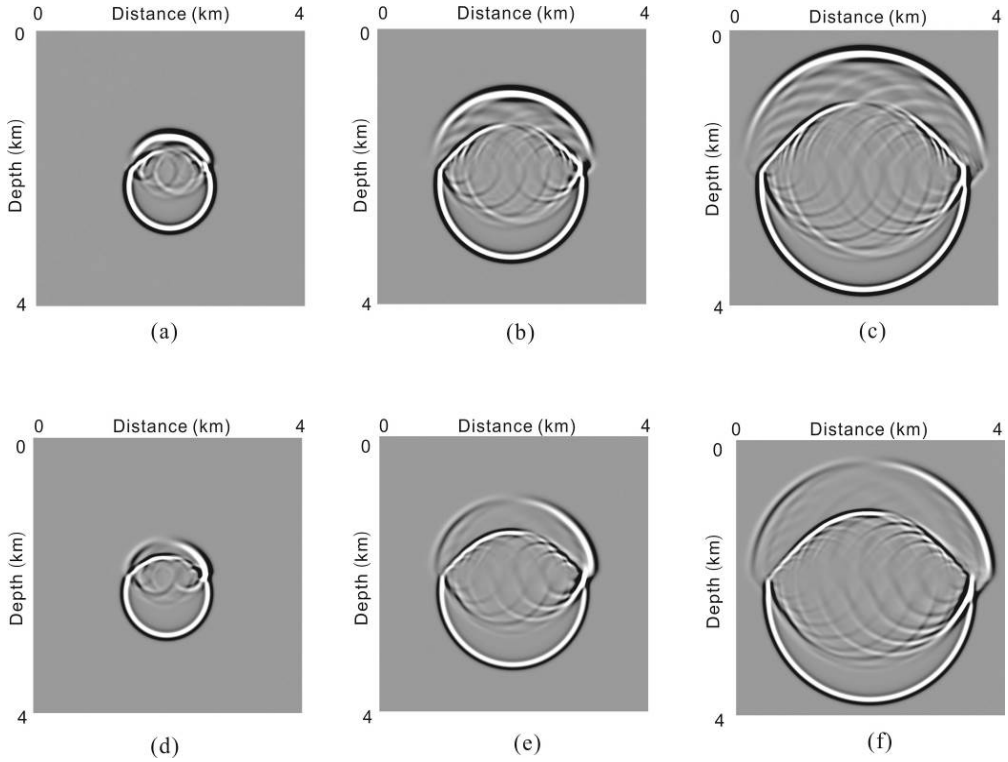

Fig. 14. Snapshots for the displacements (u_1, u_2) in the sinusoidal acoustic-elastic interface model at time $T = 0.5$ s, $T = 0.8$ s and $T = 1.1$ s. (a) and (d) are the snapshots for $T = 0.5$ s; (b) and (e) are the snapshots for $T = 0.8$ s: (c) and (f) are the snapshots for $T = 1.1$ s.

CONCLUSION

A high-order weighted Runge-Kutta Discontinuous Galerkin Method for solving 2D seismic wave equations is proposed in this paper, which extends the existing first-order and second-order methods (He et al., 2015) to higher-order cases. This method combines the DG spatial discretization and the semi-implicit solver, with the goal of improving the CFL stability conditions of the DGM and permitting the use of a larger time step.

The analyses illustrated that the proposed method achieves the expected (κ+1)-th order of spatial accuracy with P^{κ} basis functions for spatial discretization. Additionally, results indicated that using coarse meshes with a high order method for wave simulations produces smaller errors and retains high accuracy, thus increasing the computational efficiency. It was also demonstrated that the proposed method can effectively suppress numerical dispersion; in particular, when $\kappa = 5$ and $S_p = 0.5$, the dispersion error is less than 5×10^{-6}, which means that the numerical dispersion is quite small. Meanwhile, the anisotropy of the numerical dispersion was very small.

Seismic wavefield simulations demonstrated that the new method can effectively suppress numerical dispersion and provide accurate solutions on a coarse mesh in isotropic and anisotropic media. Additionally, the simulation of a cave model with strong velocity contrast confirmed the validity when applied to complex geological structures on irregular meshes. Results for a rough acoustic-elastic interface indicated that the proposed method performs excellently when applied to fluid-solid interface problems without additional or special treatments. Therefore, in the authors' view, this new method is a significant development in wave propagation modeling, particularly with regard to simulations in complex media and geometries. Although the new method produces smaller numerical dispersion on the coarse grid, its computational speed is much slower than the FDM. Therefore, computational improvements will be investigated in future research.

ACKNOWLEDGMENTS

This work was supported by the Hainan Provincial Natural Science Foundation of China (Grant Nos. 418QN205, 20161001 and 617079), Hainan Association of Science and Technology Plans for Youth Innovation (Grant No. 201503), the National Natural Science Foundation of China (Grant Nos. 41604090, 11601109) and by the Statoil Company (Contract No. 4503294711).

REFERENCES

Aki, K. and Richards, P.G., 2002. Quantitative Seismology. W.H. Freeman. & Co., Sausalito.

Ainsworth, M., Monk, P. and Muniz, W., 2006. Dispersive and dissipative properties of discontinuous Galerkin finite element methods for the second-order wave equation. J. Scientif. Comput., 27: 5-40.

Arnold, D.N., Brezzi, F., Cockburn, B. and Marini, L.D., 2002. Unified analysis of discontinuous Galerkin methods for elliptic problems. SIAM J. Numer. Analys., 39: 1749-1779.

Chaljub, E., Moczo, P., Tsuno, S., Bard, P.-Y., Kristek, J., Käser, M., Stupazzini, M. and Kristekova, M., 2010. Quantitative comparison of four numerical predictions of 3D ground motion in the Grenoble Valley, France. Bull. Seismol. Soc. Am., 100: 1427-1455.

Chen, J. and Liu, Q.H., 2013. Discontinuous Galerkin time-domain methods for multiscale electromagnetic simulations: A review. Proc. IEEE, 101: 242-254.

Cockburn, B. and Shu, C.-W., 1989. TVB Runge-Kutta local projection discontinuous Galerkin finite element method for conservation laws. II. General framework. Mathemat. Computat., 52: 411-435.

Cockburn, B. and Shu, C.-W., 2001. Runge–Kutta discontinuous Galerkin methods for convection-dominated problems. J. Scient. Comput., 16: 173-261.

Dablain, M.A., 1986. The application of high-order differencing to the scalar wave equation. Geophysics, 51: 54-66.

De Basabe, J.D. and Sen, M.K., 2010. Stability of the high-order finite elements for acoustic or elastic wave propagation with high-order time stepping. Geophys. J. Internat., 181: 577-590.

De Basabe, J.D., Sen, M.K. and Wheeler, M.F., 2008. The interior penalty discontinuous Galerkin method for elastic wave propagation: grid dispersion. Geophys. J. Internat., 175: 83-93.

de la Puente, J., Ampuero, J.P. and Käser, M., 2009. Dynamic rupture modeling on unstructured meshes using a discontinuous Galerkin method. J. Geophys. Res., Solid Earth: 114.

Dolejší, V., Holík, M. and Hozman, J., 2011. Efficient solution strategy for the semi-implicit discontinuous Galerkin discretization of the Navier–Stokes equations. J. Comput. Phys., 230: 4176-4200.

Dumbser, M. and Munz, C.-D., 2005. ADER discontinuous Galerkin schemes for aeroacoustics. Compt. Rend. Mécan., 333: 683-687.

Etienne, V., Chaljub, E., Virieux, J. and Glinsky, N., 2010. An hp-adaptive discontinuous Galerkin finite-element method for 3-D elastic wave modelling. Geophys. J. Internat., 183: 941-962.

Hairer, E., Norsett, S.P. and Wanner, G., 2006. Solving ordinary differential equations:nonstiff problems. Springer-Verlag.

He, X. , Yang, D. and Zhou, Y., 2014. A weighted Runge–Kutta discontinuous Galerkin method for wavefield modelling. Expanded Abstr., 84th Ann. Internat. SEG Mtg., Denver.

He, X., Yang, D. and Wu, H., 2015. A weighted Runge–Kutta discontinuous Galerkin method for wavefield modelling. Geophys. J. Internat., 200: 1389-1410.

He, X., Yang, D., Ma, X. and Lang, C., 2019. Dispersion-dissipation analysis of the triangle-based discontinuous Galerkin method for scalar wave equation. Geophys. J. Internat., 218: 1174-1198.

Hesthaven, J.S. and Warburton, T., 2007. Nodal Discontinuous Galerkin Methods: Algorithms, Analysis, and Applications. Springer Science and Business Media, New York.

Hu, F.Q., Hussaini, M. and Rasetarinera, P., 1999. An analysis of the discontinuous Galerkin method for wave propagation problems. J. Computat. Phys., 151: 921-946.

Käser, M. and Dumbser, M., 2006. An arbitrary high-order discontinuous Galerkin method for elastic waves on unstructured meshes - I. The two-dimensional isotropic case with external source terms. Geophys. J. Internat., 166: 855-877.

Käser, M. and Dumbser, M., 2008. A highly accurate discontinuous Galerkin method for complex interfaces between solids and moving fluids. Geophysics, 73: T23-T35.

Komatitsch, D. and Tromp, J., 1999. Introduction to the spectral element method for three-dimensional seismic wave propagation. Geophys. J. Internat., 139: 806-822.

Lambrecht, L., Lamert, A., Friederich, W., Möller, T. and Boxberg, M., 2017. A nodal discontinuous Galerkin approach to 3-D viscoelastic wave propagation in complex geological media. Geophys. J. Internat., 212: 1570-1587.

LeVeque, R.J., 2002. Finite volume methods for hyperbolic problems. Cambridge University Press, Cambridge.

Marfurt, K.J., 1984. Accuracy of finite-difference and finite-element modeling of the scalar and elastic wave equations. Geophysics, 49: 533-549.

Minisini, S., Zhebel, E., Kononov, A. and Mulder, W.A., 2013. Local time stepping with the discontinuous Galerkin method for wave propagation in 3D heterogeneous media. Geophysics, 78: T67-T77.

Moczo, P., Kristek, J. and Halada, L., 2000. 3D Fourth-order staggered-grid finite-difference schemes. Stability and grid dispersion. Bull. Seismol. Soc. Am., 90: 587-603.

Pelties, C., Puente, J., Ampuero, J.P., Brietzke, G.B. and Käser, M., 2012. Three‐dimensional dynamic rupture simulation with a high‐order discontinuous Galerkin method on unstructured tetrahedral meshes. J. Geophys. Res.: Solid Earth, 117.

Reed, W.H. and Hill, T., 1973. Triangular mesh methods for the neutron transport equation. Los Alamos Scientific Lab., NM, U.S.A.

Renac, F., Marmignon, C. and Coquel, F., 2012. Time implicit high-order discontinuous galerkin method with reduced evaluation cost. SIAM J. Scient. Comput., 34: A370-A394.

Riviere, B. and Wheeler, M.F., 2003. Discontinuous finite element methods for acoustic and elastic wave problems. Contemp. Mathemat., 329: 271-282.

Segawa, H., Luo, H. and Nourgaliev, R., 2011. A Diagonally Implicit Runge-Kutta Method for the Discontinuous Galerkin Solutions of the Navier-Stokes Equations. 49th AIAA Aerospace Sciences Mtg. including the New Horizons Forum and Aerospace Expos., 685.

Tong, P., Chen, C.-W., Komatitsch, D., Basini, P. and Liu, Q., 2014. High-resolution seismic array imaging based on an SEM-FK hybrid method. Geophys. J. Internat., 197: 369-395.

Virieux, J., 1986. P-SV wave propagation in heterogeneous media: velocity-stress finite-difference method. Geophysics, 51: 1933-1942.

Wang, N. and Zhou, Y., 2014. A weak dispersion 3D wave field simulation method: A predictor-corrector method of the implicit Runge-Kutta scheme. J. Seismic Explor., 23: 431-462.

Yang, D., Peng, J., Lu, M. and Terlaky, T., 2006. Optimal nearly analytic discrete approximation to the scalar wave equation. Bull. Seismol. Soc. Am., 96: 1114-1130.

Yang, D., Wang, N. and Liu, E., 2012. A strong stability-preserving predictor-corrector method for the simulation of elastic wave propagation in anisotropic media. Commun. Computat. Phys., 12: 1006-1032.

Zhang, J., 1997. Quadrangle-grid velocity-stress finite-difference method for elastic-wave-propagation simulation. Geophys. J. Internat., 131: 127-134.

APPENDIX A

VON NEUMANN ANALYSIS

Here we apply the Von Neumann analysis for the high order weighted Runge-Kutta Discontinuous Galerkin Method to discuss its stability and numerical dispersion. The whole analysis process is completely similar to that for the low-order case, which has been presented in detail in He et al. (2015, 2019). Here, we outline this analysis to make the paper more complete. Note that in the following analysis the high-order space basis functions are used.

We focus on the 2D acoustic wave equation for an isotropic media. Furthermore, we suppose that the medium is unbounded and source-free. These hypotheses have been widely used by Hu et al. (1999), Ainsworth et al. (2006), De Basabe et al. (2008), De Basabe and Sen (2010). We recall that the flux $F(W)$ is linear, then we rewrite it as:

$$F(W) = (A_1 W, A_2 W),$$

where

$$A_1 = \begin{bmatrix} 0 & -c^2 & 0 \\ -1 & 0 & 0 \\ 0 & 0 & 0 \end{bmatrix}, \quad A_2 = \begin{bmatrix} 0 & 0 & -c^2 \\ 0 & 0 & 0 \\ -1 & 0 & 0 \end{bmatrix}.$$

We divide the domain into rectangular element $E^{nm} = [x_n, x_{n+1}] \times [z_m, z_{m+1}]$, with each side of length h. Let $\boldsymbol{C}^{nm}(t) = (C_1^{nm}, C_2^{nm}, \mathrm{K}, C_{d_{loc}}^{nm})^{\mathrm{T}}$, then eq. (9) or (10) can be written as (Hu et al., 1999):

$$\begin{aligned} \boldsymbol{Q}\frac{\partial \boldsymbol{C}^{nm}}{\partial t} &+ \frac{2}{h}[\boldsymbol{N}_0 \boldsymbol{C}^{nm} + \boldsymbol{N}_{-1}\boldsymbol{C}^{n-1m} + \boldsymbol{N}_{+1}\boldsymbol{C}^{n+1m}] \\ &+ \frac{2}{h}[\boldsymbol{M}_0 \boldsymbol{C}^{nm} + \boldsymbol{M}_{-1}\boldsymbol{C}^{nm-1} + \boldsymbol{M}_{+1}\boldsymbol{C}^{nm+1}] = 0 \end{aligned}, \tag{A-1}$$

where the explicit forms of these matrices are shown in Appendix B.

We assume that the solution is a plane wave in the form

$$\boldsymbol{C}^{nm}(t) = \boldsymbol{C}(t)\exp[\mathrm{i}(k\cos\theta nh + k\sin\theta mh)] \quad ,$$

where k denotes the wave number and θ denotes the propagation angle. By substituting the wave expression into eq. (A-1), we get

$$\frac{\partial \boldsymbol{C}(\mathrm{t})}{\partial t} = -\boldsymbol{Q}^{-1}\left[\frac{2}{h}(\boldsymbol{N}_0 + \boldsymbol{N}_{-1}\mathrm{e}^{-\mathrm{i}k\cos\theta h} + \boldsymbol{N}_{+1}\mathrm{e}^{\mathrm{i}k\cos\theta h}) + \frac{2}{h}(\boldsymbol{M}_0 + \boldsymbol{M}_{-1}\mathrm{e}^{-\mathrm{i}k\sin\theta h} + \boldsymbol{M}_{+1}\mathrm{e}^{\mathrm{i}k\sin\theta h})\right]\boldsymbol{C}(\mathrm{t}) \quad . \tag{A-2}$$

We introduce a variable $\boldsymbol{S}$ to simplify the right hand side of eq. (A-2), which is written as:

$$\frac{\partial \boldsymbol{C}(\mathrm{t})}{\partial t} = \boldsymbol{S}\boldsymbol{C}(\mathrm{t}) \quad , \tag{A-3}$$

where

$$\boldsymbol{S} = -\boldsymbol{Q}^{-1}\left[\frac{2}{h}(\boldsymbol{N}_0 + \boldsymbol{N}_{-1}\mathrm{e}^{-\mathrm{i}k\cos\theta h} + \boldsymbol{N}_{+1}\mathrm{e}^{\mathrm{i}k\cos\theta h}) + \frac{2}{h}(\boldsymbol{M}_0 + \boldsymbol{M}_{-1}\mathrm{e}^{-\mathrm{i}k\sin\theta h} + \boldsymbol{M}_{+1}\mathrm{e}^{\mathrm{i}k\sin\theta h})\right] \quad .$$

Then, we discretize eq. (A-3) using the time discretization scheme discussed above. After some algebra, we obtain:

$$\boldsymbol{C}^{n+1} = \left(I + \frac{\Delta t}{2}(G_1 + G_1 G_2)\right)\boldsymbol{C}^n \quad , \tag{A-4}$$

where $G_1 = \boldsymbol{S} + r\Delta t\boldsymbol{S}^2 + \eta(r\Delta t)^2\boldsymbol{S}^3$, $G_2 = I + (1-2r)\Delta t G_1$.

Next, we let $\boldsymbol{C}^n = \boldsymbol{C}^0\mathrm{e}^{-\mathrm{i}\omega n\Delta t}$, where ω is the numerical angular frequency, and $\boldsymbol{C}^0$ is an constant vector. Thus, eq. (A-4) could be written as:

$$\mathrm{e}^{-\mathrm{i}\omega\Delta t}\boldsymbol{C}^0 = \left(\boldsymbol{I} + \frac{\Delta t}{2}(G_1 + G_1 G_2)\right)\boldsymbol{C}^0 \quad . \tag{A-5}$$

Taking Λ be an eigenvalue of the matrix on the right-hand side of eq. (A-5), we have

$$\mathrm{e}^{-\mathrm{i}\omega\Delta t} = \Lambda \quad . \tag{A-6}$$

In general, Λ and ω are complex numbers. Λ relates to the numerical stability and ω relates to the numerical dispersion. We denote $\omega = \omega_r + \mathrm{i}\omega_i$ and $\Lambda = \Lambda_r + \mathrm{i}\Lambda_\mathrm{i}$, in which the superscripts i and r correspond to the real part and imaginary part, respectively. ω_r and ω_i are related to the numerical

dispersion and numerical dissipation, respectively. With the decompositions of Λ and ω into eq. (A-6), we get:

$$\Lambda_r + \mathrm{i}\Lambda_\mathrm{i} = \mathrm{e}^{-\mathrm{i}(\omega_r + \mathrm{i}\omega_i)\Delta t} = \mathrm{e}^{\omega_i \Delta t}(\mathrm{e}^{-\mathrm{i}\omega_r \Delta t}) = \mathrm{e}^{\omega_i \Delta t}\left(\cos(\omega_r \Delta t) - \mathrm{i}\sin(\omega_r \Delta t)\right) \quad .$$

Solving for $\omega_r \Delta t$, we then get:

$$\omega_r \Delta t = \arctan(-\frac{\Lambda_\mathrm{i}}{\Lambda_r}) \quad .$$

The numerical dispersion R is defined as the ratio of numerical velocity c_{num} and physical velocity c. If we adopt the definition of the spatial sampling ratio proposed by Moczo et al. (2000): $S_p = h/\lambda = kh/(2\pi)$, then we get:

$$R = \frac{c_{\mathrm{num}}}{c} = \frac{\omega_r}{ck} = \frac{\omega_r \Delta t}{\alpha kh} = \frac{\omega_r \Delta t}{2\pi\alpha S_p} .$$

APPENDIX B

THE MATRIX EXPRESSIONS IN EQ. (A-1)

Hu et al. (1999) gave detailed expressions for the matrices used in eq. (A-1) in the 2D case. The time-independent polynomial basis functions, denoted as $\{w_l(x,z)\big|l = 0,1,\mathrm{K}\ ,d_{loc}-1\}$, are defined on the reference element $E = [-1,1]\times[-1,1]$. For example, for the Legendre basis functions, $\{w_l(x,z)\big|l = 0,1,\mathrm{K}\ ,d_{loc}-1\}$ are:

$$\left\{1, x, z, xz, \frac{3}{2}x^2 - \frac{1}{2}, \frac{3}{2}z^2 - \frac{1}{2}, \mathrm{K}\right\}$$

d_{loc} is the total number of the basis functions in element E. The entries of the matrices in eq. (A-1) are:

$$\{\boldsymbol{N}_0\}_{ij} = \left\{\frac{A_1 + C_{L_1} I}{2}\right\}_{\alpha\beta} \int_{-1}^{1} w_{l'}(1,y) w_l(1,y)\,\mathrm{d}y - \left\{\frac{-A_1 + C_{L_3} I}{2}\right\}_{\alpha\beta} \int_{-1}^{1} w_{l'}(-1,y) w_l(-1,y)\,\mathrm{d}y$$
$$- \{A_1\}_{\alpha\beta} \int_{-1}^{1}\int_{-1}^{1} \frac{\partial w_{l'}}{\partial x} w_l \,\mathrm{d}x\mathrm{d}y$$

$$\{\boldsymbol{N}_{+1}\}_{ij} = \left\{\frac{A_1 - C_{L_1} I}{2}\right\}_{\alpha\beta} \int_{-1}^{1} w_{l'}(1,y) w_l(-1,y)\,\mathrm{d}y,$$

$$\{\boldsymbol{N}_{-1}\}_{ij} = \left\{\frac{-A_1 - C_{L_3} I}{2}\right\}_{\alpha\beta} \int_{-1}^{1} w_{l'}(1,y) w_l(-1,y)\,\mathrm{d}y,$$

$$\{\boldsymbol{M}_0\}_{ij} = \left\{\frac{A_2 + C_{L_2} I}{2}\right\}_{\alpha\beta} \int_{-1}^{1} w_{l'}(x,1) w_l(x,1)\,\mathrm{d}y - \left\{\frac{-A_2 + C_{L_4} I}{2}\right\}_{\alpha\beta} \int_{-1}^{1} w_{l'}(x,-1) w_l(x,-1)\,\mathrm{d}y$$
$$- \{A_2\}_{\alpha\beta} \int_{-1}^{1}\int_{-1}^{1} \frac{\partial w_{l'}}{\partial y} w_l \,\mathrm{d}x\mathrm{d}y$$

,

$$\{\boldsymbol{M}_{+1}\}_{ij} = \left\{\frac{A_2 - C_{L_2} I}{2}\right\}_{\alpha\beta} \int_{-1}^{1} w_{l'}(x,1) w_l(x,-1)\,\mathrm{d}x,$$

$$\{\boldsymbol{M}_{-1}\}_{ij} = \left\{\frac{-A_2 - C_{L_4} I}{2}\right\}_{\alpha\beta} \int_{-1}^{1} w_{l'}(x,-1) w_l(x,1)\,\mathrm{d}x,$$

where

$$\delta_{\alpha\beta} = \begin{cases} 1 & \text{if } \alpha = \beta \\ 0 & \text{otherwise} \end{cases}$$

and $i = ml' + \alpha, j = ml + \beta;\ \alpha, \beta = 0,1,\mathrm{K}\ m-1;\ l', l = 0,1,\mathrm{K}\ , d_{loc} - 1$, in which d_{loc} is the number of the basis function set defined on the reference rectangular element, and *m* is the number of the unknown variables in W.